Accepted Manuscript

Ultrasound-assisted impregnation for high temperature Fischer-Tropsch catalysts

Paul Louyot, Cristian Neagoe, Federico Galli, Carlo Pirola, Gregory S. Patience, Daria C. Boffito

PII: S1350-4177(18)30750-8
DOI: https://doi.org/10.1016/j.ultsonch.2018.06.017
Reference: ULTSON 4215

To appear in: *Ultrasonics Sonochemistry*

Received Date: 16 May 2018
Revised Date: 20 June 2018
Accepted Date: 20 June 2018

Please cite this article as: P. Louyot, C. Neagoe, F. Galli, C. Pirola, G.S. Patience, D.C. Boffito, Ultrasound-assisted impregnation for high temperature Fischer-Tropsch catalysts, *Ultrasonics Sonochemistry* (2018), doi: https://doi.org/10.1016/j.ultsonch.2018.06.017

This is a PDF file of an unedited manuscript that has been accepted for publication. As a service to our customers we are providing this early version of the manuscript. The manuscript will undergo copyediting, typesetting, and review of the resulting proof before it is published in its final form. Please note that during the production process errors may be discovered which could affect the content, and all legal disclaimers that apply to the journal pertain.

ACCEPTED MANUSCRIPT

Ultrasound-assisted impregnation for high temperature Fischer-Tropsch catalysts

Paul Louyot[a], Cristian Neagoe[a], Federico Galli[a,b], Carlo Pirola[b], Gregory S. Patience[a], Daria C. Boffito[a,*]

[a] *Department of Chemical Engineering, Polytechnique Montréal, 2500, chemin de Polytechnique, Montréal, H3T 1J4 Québec, Canada*
[b] *Dipartimento di Chimica, Università degli Studi di Milano, via Golgi 19, 20133, Milano, Italy*

Abstract

A fraction of the petroleum extracted from oil reservoirs contains associated natural gas. Rather than building infrastructure to recover low volumes of this natural gas, the industry flares or vents it to the atmosphere, which contributes to atmospheric greenhouse gas emissions but also reduces the air quality locally because it contains gaseous sulphur and nitrogen compounds. Converting the natural gas (NG) to hydrocarbons with a small-scale two-step gas-to-liquids process, is an alternative to flaring and venting. In the first step, NG reacts with oxygen to form syngas (Catalytic Partial Oxidation) and in the second step the syngas reacts over metallic catalysts to form higher paraffins at 210 °C to 300 °C—Fischer Tropsch synthesis (FT). For the first time, we synthesize bimetallic FeCo FT catalysts with ultrasound. An ultra-

*Corresponding author
Email address: daria-camilla.boffito@polymtl.ca (Daria C. Boffito)

ACCEPTED MANUSCRIPT

sonic horn agitates the solution during the entire impregnation process. The active phase dispersion of the sonicated catalysts was superior to the catalyst synthesized without ultrasound, while reducing the impregnation time by a factor of three. We tested our catalysts in a lab-scale, fixed-bed reactor at 270 °C and 300 °C achieved 80 % conversion over 3-days on stream, and a 40 % yield of C_{2+}.

Keywords: Fischer-Tropsch, catalyst synthesis, impregnation, sonocatalysis, ultrasound, iron, FeCo

1. Introduction

Natural gas is a co-product of oil extraction and is problematic when the volumes are too low to justify investing in infrastructure to transport it. Conveying natural gas by pipeline is uneconomic for remote oil wells as it costs 100 000 $/mile per inch in diamter of pipe (a 3 inch diameter pipe costs 300 000 $/kmile) [1]. As a result, the yearly world wide environmental burden related to gas flaring while producing petroleum is more than 300 million tons of CO_2 [2].

An alternative to flaring is to convert natural gas in-situ to a liquid product in a mobile, integrated gas to liquids unit (GtL) [3]. Patience and Boffito patented a double stage reactor housed in a single pressure vessel that produces synthesis gas (syngas) by catalytic partial oxidation of methane at temperatures >900 °C, followed by Fischer-Tropsch (FT) at 300 °C [4, 5]. In the Fischer-Tropsch synthesis, Co and

ACCEPTED MANUSCRIPT

Fe-based catalysts convert H_2 and CO into hydrocarbons [6]:

Alkanes production:

$(2n+1)\,H_2 + nCO \rightarrow C_nH_{2n+2} + n\,H_2O$

Alkenes production:

$2n H_2 + nCO \rightarrow C_nH_{2n} + n\,H_2O$

Alcohols production:

$(2\,n\text{-}1)\,H_2 + n\,CO \rightarrow C_nH_{2n-1}OH + (n\text{-}1)H_2O$

Dry and co-authors identified catalyst formulation as one of the most important variables for the viability of the FT process [7]. The active phase usually contains at least one metal of groups VIII, IX, X of the periodic table [8]. Because of their relatively low-price and high activity, Fe and Co-based catalysts are the most common. Fe based catalysts operate over a wider range of temperature, pressure and space velocity, and under extreme conditions its activity can match and exceed that of Co based catalysts that operate at low temperature. On the negative side, Fe promotes the water gas shift reaction ($CO + H_2O \rightarrow H_2 + CO_2$). However, when operating at conversions lower than 30 % the contribution of the water gas shift reaction of a Fe catalyst compared to a Co catalyst becomes almost the same, eliminating the advantages of the latter [9].

Fe is three orders of magnitude less expensive than Co and produces less methane,

ACCEPTED MANUSCRIPT

but Co catalysts have a turnover frequency three times greater [10] and are more resistant to deactivation by water [11, 12]. Literature studies on FeCo alloys are sparse but they appear to convert more CO compared to monometallic catalysts. Arai et al. tested several Fe/Co bimetallic and monometallic catalysts supported over TiO_2 at 250 °C. The catalyst with 50 %(Fe)50 %(Co) with a total metal loading of 10 % converted the most CO at 46 % [13]. De la Peña O'Shea et al. designed a catalyst with 10 % Co and 5 % Fe over silica that converted 76 % CO at 260 °C [14]. In bimetallic systems, Co increases the fraction of metallic Fe after reduction [15]. At low temperature, i.e. 200-250 °C, the catalyst activity increases with Co content [16].

In the mobile GtL unit patent, oxygen partially oxidizes CH_4 to syngas at 1000 °C so maximizing the Fischer-Tropsch reaction temperature reduces the cooling duty between the two steps. Thus temperatures above 300 °C are favoured compared to the low temperature Co process while bimetallic systems have never been tested at temperatures higher than 250 °C.

Researchers have tested incipient wetness impregnation, co-impregnation, and deposition-precipitation methods to make FT catalysts [11]. Duvenhage and Coville prepared Fe/Co catalysts via impregnation and co-impregnation from various precursors. They observed a Fe-Co synergy that was independent of the synthesis method.

ACCEPTED MANUSCRIPT

However, samples impregnated from carbonyl precursors were in some cases even twice as active as the samples obtained by co-precipitation [17]. Catalyst activity increases with the metal loading [18, 19]. To achieve high metal loadings, traditional methods require several impregnation steps, which take up to 24 h [20, 21].

Ultrasound (US) improves mass transfer and intensifies chemical reactions [22–24]. Sonochemistry takes advantage of the particular conditions created by the implosion of cavitation bubbles, which generates hot-spots: sites of extreme pressure and temperature ($T > 4000\,\mathrm{K}$, $P > 100\,\mathrm{MPa}$). Sonicating a solution during impregnation increases the mass transport of precursors, thus reducing synthesis time [25], may stabilize nanophases [26], increase specific surface area [22] and tune porosity [27]. **(author?)** [28] synthesized Ag catalysts supported on TiO_2 and reported an increased metal loading on the outer surface of the catalyst vs. the internal surface area, compared to catalysts with traditional impregnation, whereby most Ag coated the inner surface.

(author?) [29] synthesized supported bimetallic catalysts assisted by US for methane reforming, and compared their activity versus samples prepared by classical impregnation. The surface of the sono-synthesized sample was regular, without active particles agglomeration, in contrast with the catalyst prepared by traditional impregnation where the surface was rough, and showed coarse agglomerations. .

ACCEPTED MANUSCRIPT

Panahi et al. prepared sonicated catalysts for NO reduction and also reported higher active phase dispersion on their sonicated catalysts [30].

Our work is original for several reasons. i) We prepare bimetallic FeCo catalysts with ultrasonic agitation during impregnation while reducing the impregnation time by a factor of three; ii)We test them at high temperature (270 °C) in a bench-scale Fischer-Tropsch reactor at short residence time of 1 s to 3 s; iii) CO conversion reached 80 % and yield to C_2^+ was 40 %, with a residence time several fold shorter than previous works [21].

The purpose of this paper is to analyze the influence of US sonication during impregnation on monometallic and bimetallic Fischer-Tropsch catalysts on their structural and morphological properties.

2. Experimental

2.1. Materials

Activated alumina Al_2O_3, metal precursors ($Fe(NO_3)_3$, $Co(NO_3)_2$) and promoters ($Cu(NO_3)_2$, K_2CO_3) were purchased from Sigma-Aldrich and were used as received without further purification.

2.2. Catalysts synthesis

We apply the following nomenclature for the bimetallic catalysts:

ACCEPTED MANUSCRIPT

$_a$Ar-x%(Fe)y%(Co)

where a is the flow rate ($\mathrm{mL\,min^{-1}}$) of Ar bubbled in the solution during impregnation, and x and y are the mass percentages of iron and cobalt. Copper and potassium are promoters—a mass percentage of 4 % and 2 % of the iron loading, respectively [21, 31]. Comazzi et al. employed iron pentacarbonyl as a precursor of the active phase [31]. Here, we chose metallic nitrates as precursors because they are less toxic [?].

We added alumina to distilled water followed by the Fe and Co salts and promoters. The total volume of the solution was 70 mL.

An 500 W ultrasound probe (nominal power) with a tip diameter $\frac{3}{4}$ inch nozzle, sonicated the solution during the impregnation (VCX 500, Sonics & Materials, Inc.). The impregnation lasted 4 h.

We measured the power delivered to the solution with Uchida and Kikuchi's calorimetric method [32]. During the impregnation, the probe delivered 25 W to the solution. The device operated in pulse mode, i.e. 2 s on, 2 s off, After impregnation, an electric furnace dried the powder for 12 h at 393 K (ramp $10\,\mathrm{K\,min^{-1}}$), reached 873 K (ramp $3\,\mathrm{K\,min^{-1}}$) and calcined it in static air for 4 h.

We prepared six samples all with the same Fe loading and a varying Co loading and argon flow rate (Table 1). In addition with the sono–synthesized samples, we

ACCEPTED MANUSCRIPT

Table 1: Design of experiment: synthesis of bi-metallic Fischer-Tropsch catalysts

Sample	Fe mass %	Co mass %	Ar $mL\,min^{-1}$
$_{00}$Ar-15%(Fe)3%(Co)	15	3	0
$_{00}$Ar-15%(Fe)15%(Co)	15	15	0
$_{10}$Ar-15%(Fe)3%(Co)	15	3	10
$_{10}$Ar-15%(Fe)15%(Co)	15	15	10
$_{10}$Ar-15%(Fe)	15	0	10
blank,15%(Fe)3%(Co)	15	3	0

synthesized a blank sample without ultrasound.

2.3. Catalysts characterization

An Autosorb-1 instrument (Quantachrome Instruments) measured the surface area and porosity of the samples at 77 K. All samples degassed overnight under vacuum at 200 °C before the analysis. The specific surface areas were calculated by the multi-point BET method with N_2 as a sorbate.

A field emission scanning electron microscope (FE-SEM-JEOL JSM-7600F) with a voltage of 5 kV imaged the powders. Scanning electron microscopy energy dispersive X-ray spectroscopy (SEM-EDS) detected the distribution of the elements in the particles. It operated at a voltage of 5 kV with an energy range of 10 keV.

An X-ray diffractometer (X'Pert) acquired the crystallographic parameters and crystal structure of the powder. The scanning range was from 10° to 80° with a step size of 0.02° and a scan rate of $0.05\,^{\circ}\,s^{-1}$.

ACCEPTED MANUSCRIPT

A Horiba (LA-950) laser diffractometer measured the mean diameter of the samples as well as the diameter distribution based on volume, i.e. it calculated the $D_M[4,3]$.

An M-Probe Instrument (SSI) for the XPS analysis, equipped with a monochromatic source $Al-K_\alpha$, measured the atomic surface composition of the samples. The calibration was made with Au (4f7/2 at 84.000 eV), the superficial charge was 2 eV. The C1s peak (284.6 eV) was the reference. The area of analysis for each sample was 1 mm per 0.4 mm. The precision was 0.2 eV, and the experimental error was 5 %.

A TGA Q50 performed the thermogravimetric analysis of the coked catalyst. The sample was placed in a platinum pan. The furnace ramped the temperature at 10 K min^{-1} up to 900 °C under air flow (10 mL min^{-1}).

2.4. Experimental bench scale tests

We evaluated catalyst activity in a fixed bed reactor 12 mm in diameter by 765 mm (Figure 1). Prior to the Fischer-Tropsch reaction, each catalyst sample was sieved 38 µm to 300 µm.

Three mass flow controllers (MFC, Brooks instruments) set the flowrate of H_2, CO, and Ar (dilution gas).

A flow of 100 SmL/min (composition 95 % H_2, 5 % Ar) activated the sample by reduction *in-situ* at 380 °C for 12 h. H_2 rather than syngas activates Co-based Fischer

ACCEPTED MANUSCRIPT

Tropsch catalysts [33]. Differently, syngas is the best choice to activate Fe catalyst since the Fe carbies are the active species [34, 35]. We decided to activate all catalyst with H_2 because of the presence of Co. We activated monometallic Fe-based catalysts with H_2 as well to keep the activation conditions constant for all catalysts.

We conducted each test with a H_2/CO ratio of 2. The residence time, τ, is the ratio between the volume of catalyst and total flow rate. A back pressure regulator maintained the reactor at 2 MPa. A type K thermocouple monitored the reactor temperature in the middle of the catalytic bed.

In a first set of tests (set A), we compared the catalytic activity of $_{10}$Ar-15%(Fe)3%(Co) and $_{10}$Ar-15%(Fe) (Table 2) at $\tau = 1.0$ s and a total flow rate of 810 SmL/min: H_2–463 SmL/min, CO–231 SmL/min, and Ar–116 SmL/min. We diluted the catalyst bed with alumina at a Al_2O_3/catalyst volume ratio = 1). Diluting the feed gas with Ar flow and the catalyst with alumina reduced the propensity to form hot spots in the bed.

In a second set of tests (set B), we studied the influence of regeneration and residence time on $_{10}$Ar-15%(Fe) catalyst (Table 2). After the test at 270 °C in set A, oxygen flow (200 mL min^{-1}, 30 % O_2, 70 % Ar) at 400 °C regenerated the catalyst. Both tests at residence time $\tau = 3$ s were performed with fresh catalyst.

An Agilent 7890B gas chromatograph (GC) analyzed light hydrocarbons and

ACCEPTED MANUSCRIPT

Table 2: Fischer-Tropsch activity tests

	Catalyst	Residence time s	Temperature °C
Set A			
	$_{10}$Ar-15%(Fe)3%(Co)	1	220
		1	270
	$_{10}$Ar-15%(Fe)	1	220
		1	270
Set B			
	$_{10}$Ar-15%(Fe) after regeneration	1	270
	$_{10}$Ar-15%(Fe)	3	270
	$_{10}$Ar-15%(Fe)	3	300

unreacted gases on-line. The oven temperature equilibrated at 50 °C for 4 min first, then it ramped up to 100 °C at 25 °C min^{-1} remained constant for 7 min. The GC was equipped with a flame ionization detector, for $C_2{}^+$ hydrocarbons, a thermal conductivity detector for CO, H_2 and CH_4, and an second thermal conductivity detector for CO_2. We calibrated the TCD with ethane and C3-C4 cylinders (Air Liquide) and the TCD with a methane bottle—mix calibration in Figure 1.

$C_7{}^+$ liquid products condensed in a cold trap (average temperature: 8 °C) and a we analyzed these compounds by GC at the end of the test. A bubblemeter measured the reactor exit flow rate. The conversion of carbon monoxyde is defined as $X_{\mathrm{CO}} = \frac{\mathrm{CO}_{in} - \mathrm{CO}_{out}}{\mathrm{CO}_{in}}$. We express product selectivity (S) in C atoms, as the percentage of CO converted into CO_2 or Ci product.

ACCEPTED MANUSCRIPT

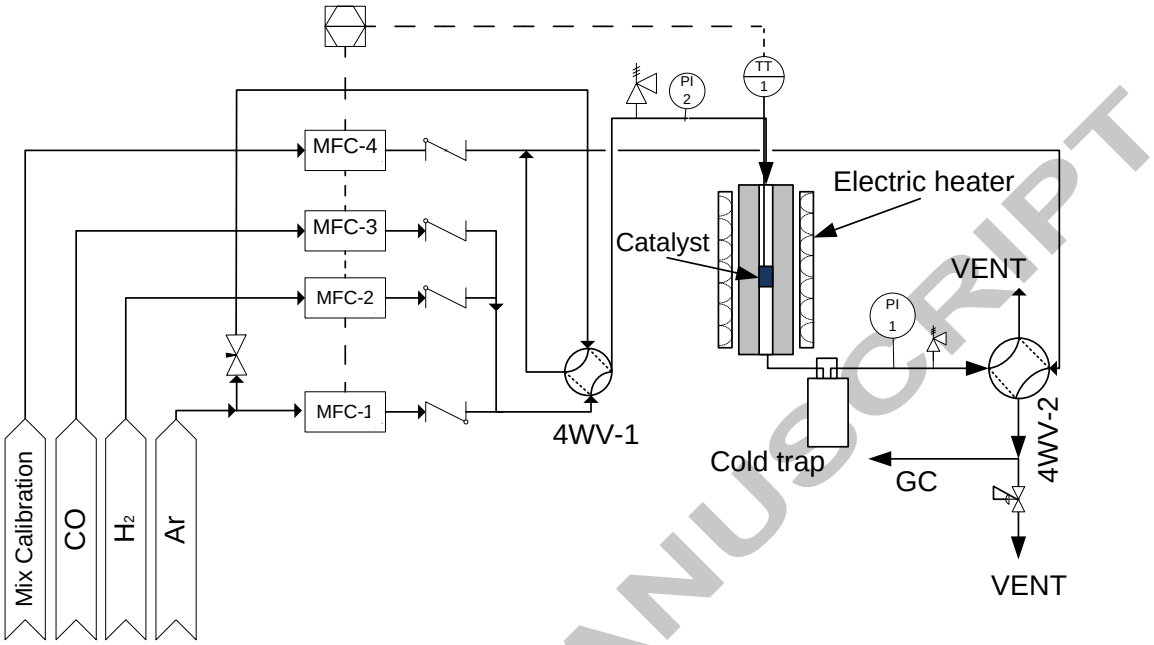

Figure 1: Fischer-Tropsch test set-up

3. Results and discussion

3.1. Catalyst characterization

3.1.1. XRD analysis

We report the XRD diffractogram of the $_{00}$Ar-15%(Fe)3%(Co) sample as a representative catalyst for the sake of brevity. The XRD profile of $_{00}$Ar-15%(Fe)3%(Co) is noisy, as a result of low intensity peaks (Figure 2). These peaks indicate that the material is amorphous, in agreement with the literature on ultrasound synthesis [36] and specifically for Fe-based samples synthesized by ultrasound [31]. However, the XRD detected peaks belonging to hematite Fe_2O_3 (JCPDS card no. 33-0664), which

ACCEPTED MANUSCRIPT

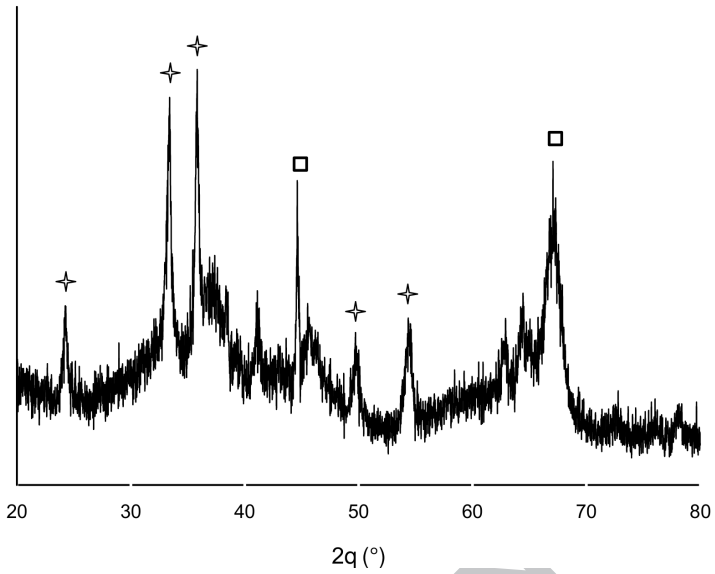

Figure 2: XRD acquisition of $_{00}$Ar-15%(Fe)3%(Co) at 50 kV and 40 mA. Star symbol peaks correspond to Fe_2O_3 (hematite). Square symbol peak corresponds to Al_2O_3 (alumina).

has a rhombohedral structure and γ-Al_2O_3.

3.1.2. BET and PSD analysis

All N_2 adsorption isotherms correspond to type IV, with H4 hysteresis category (Figure 3) according to the IUPAC classification [37]. This is characteristic of slit-like, mesoporous cavities.

We measured the particle size distribution 5 times for $_{00}$Ar-15%(Fe)3%(Co), $_{10}$Ar-15%(Fe)3%(Co) and blank,15%(Fe)3%(Co) (Table 3). The mean difference between $_{00}$Ar-15%(Fe)3%(Co) and blank,15%(Fe)3%(Co) is statistically significant (p-value = 0.0019), and is the case between $_{00}$Ar-15%(Fe)3%(Co) and $_{10}$Ar-15%(Fe)3%(Co)

ACCEPTED MANUSCRIPT

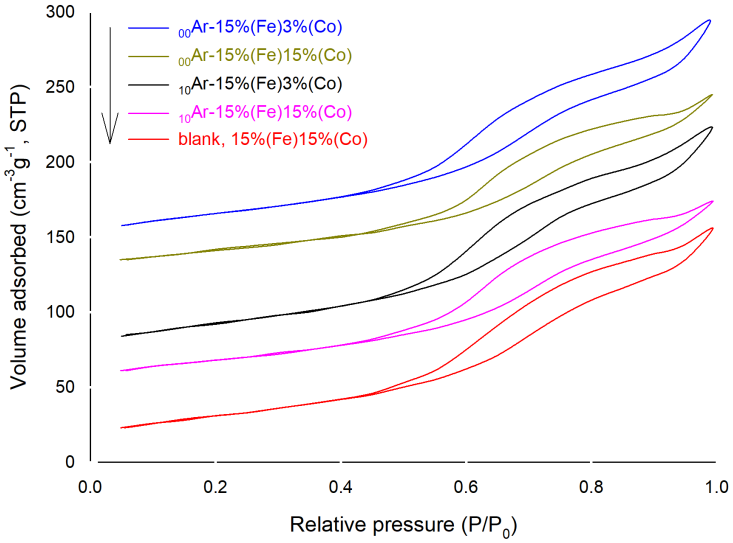

Figure 3: Nitrogen adsorption and desorption: Volume at standard temperature and pressure (cc/g) as a function of relative pressure, where a) is $_{00}$Ar-15%(Fe)3%(Co), b) is $_{00}$Ar-15%(Fe)15%(Co), c) is $_{10}$Ar-15%(Fe)3%(Co), d) is $_{10}$Ar-15%(Fe)15%(Co) and e) is the blank,15%(Fe)3%(Co).

(p-value $= 0.011$) so we can reject the null hypothesis that the means are the same and thus accept the alternative that u ltrasound reduces the mean particle size, However, Ar bubbling dampens this reduction when both Fe and Co are supported as the difference between the means blank,15%(Fe)3%(Co)and $_{10}$Ar-15%(Fe)3%(Co)are insignificant. Ar bubbling increases the violence of the cavitation implosions, which decreases the median diameter but increases the local temperature, which sinters the particles more. Here, the latter effect dominates the catalyst synthesis. However, this effect in catalyst with only one metal ($_{10}$Ar-15%(Fe)).

The BET-N_2 surface area decreases with the total metal loading due to metal

ACCEPTED MANUSCRIPT

Table 3: Particle median diameter (d_{50}), specific surface area (BET-N_2) and total pore volume (V_{pore}) of synthesized samples. Sample standard devitations, s, are based on 5 samples for the PSD and 3 samples for the BET.

sample	d_{50} µm	$s_{d_{50}}$ µm	BET-N_2 $m^2\,g^{-1}$	s_{BET} $m^2\,g^{-1}$	V_{pore} $cm^3\,g^{-1}$
blank,15%(Fe)3%(Co)	82	1.7	112		2.4
$_{00}$Ar-15%(Fe)3%(Co)	68	5.0	110	1.4	2.5
$_{00}$Ar-15%(Fe)15%(Co)	64		94	1.1	2
$_{10}$Ar-15%(Fe)3%(Co)	78	4.6	117	1.4	2.5
$_{10}$Ar-15%(Fe)15%(Co)	84		101		2.1
$_{10}$Ar-15%(Fe)	61		115		

fills the pores of the support as well as the dilution effect: the surface area of the metal is much lower than the support so adding metal increases the mass without contributing to the overall surface area. The BET-nitrogen surface area increases bubbling Ar in the slurry during impregnation. Ar increases the number of shock waves, producing more surface erosion and increasing the surface area as a result of intensified cavitation in the solution. The total pore volume follows the same trend as the specific surface area.

We repeated the surface area measurements for samples $_{00}$Ar-15%(Fe)3%(Co) and $_{10}$Ar-15%(Fe)3%(Co) three times. The difference between the mean values is statistically significant (p-value = 0.0032).

ACCEPTED MANUSCRIPT

3.1.3. SEM-EDX analysis

We compared catalysts impregnated 1) with ultrasound without Ar bubbling (4a, 4b) 2) with ultrasound with Ar bubbling (4c, 4d) and 3) without either ultrasound assistance or Ar bubbling (4e, 4f).

The size of catalyst particles is coherent with the PSD analysis (Figure 4). Ultrasound decreases the particle size of the samples, but when Ar bubbles in the presence of ultrasound, the particle size of the samples containing both Co and Fe increases because of syntering.

Ultrasound clearly erodes the outer surface of the samples (4a-4d vs. 4e-4f). We added Ar to intensify the impact of the ultrasound shock waves on the support being impregnated. Catalysts synthesized in the presence of Ar (4a-4b) have a more spherical shape and rougher outer surface compared to catalysts synthesized without Ar (4c-4d), which still have a rough outer surface but are an ensemble of aggregates. Also the particles of the blank samples are aggregates or smaller crystallites, but their surface is paved. However, even if the outer surface is rougher, the specific surface area does not increase because the particles are bigger.

We rationalize these results considering cavitation bubbles characteristics. Images 4c, and 4d refer to a solution in which Ar is the main gas dissolved during the synthesis. Without Ar, N_2 and O_2, even though in much smaller concentration,

ACCEPTED MANUSCRIPT

(a) $_{00}$Ar-15%(Fe)3%(Co) (b) $_{00}$Ar-15%(Fe)15%(Co)

(c) $_{10}$Ar-15%(Fe)3%(Co) (d) $_{10}$Ar-15%(Fe)15%(Co)

(e) blank,15%(Fe)3%(Co) (f) blank,15%(Fe)3%(Co)

Figure 4: SEM pictures of samples sonicated without (4a,4b) and with (4c,4d) Ar bubbling, as well as the blank sample impregnated without ultrasounds (4e,4f). Pictures 4e and 4f originate from the same sample.

predominate. The adiabatic index, γ, of monatomic gases like Ar is 1.66 while it is only 1.4 for diatomic gases like N_2 and O_2 The maximum temperature reached inside the bubble depends on γ (Eq. 1):

$$T_{max} = T_0 \left[\frac{P_m(\gamma - 1)}{P} \right] \quad (1)$$

where T_0 is the ambient reaction temperature, P is the gas pressure inside the bubble at its maximum size, P_m is the liquid pressure at bubble collapse and γ is the adiabatic index [38]. The maximum temperature is the highest inside Ar bubbles, which favours particle syntering.

SEM images of the sonicated samples show a film of small particles with large agglomerates underneath (Figure 4), whereas the blank sample only show large agglomerates of active phase. Argon bubbling during impregnation does not influence significantly the repartition of the metallic sites on the support.

ACCEPTED MANUSCRIPT

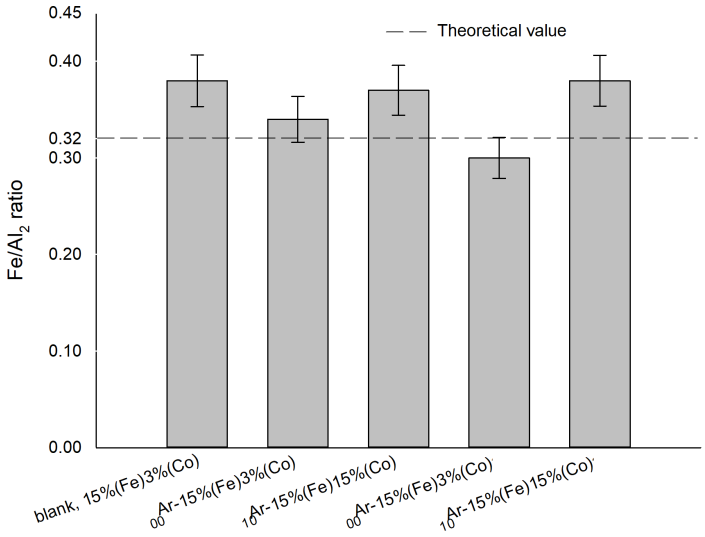

Figure 5: XPS Fe/Al_2 atomic ratios. The error bars represent the experimental error of the instrument.

3.1.4. XPS analysis

From the XPS analysis, we calculated the atomic Fe/Al_2 ratio of the calcinated samples. It is similar to one calculated with the stoichiometry of the reagents (Figure 5). FeO peak exceeds 710 eV and presents an Auger peak at 784 eV that covers the 2p3/2 e 2p1/2 signals of Co. Thus, a determination of the superficial Co content is not possible.

ACCEPTED MANUSCRIPT

3.2. Activity tests

3.2.1. Experimental tests: set A

Tests A all refer to a residence time of 1 s. Among the four bimetallic catalysts, $_{10}$Ar-15%(Fe)3%(Co) had the highest specific surface area, correlated with the second highest particle size (Table 3), hence we selected this sample for the test in the fixed bed. We also tested the monometallic catalyst $_{10}$Ar-15%(Fe) with the same ratio of Fe to investigate the effect of combining Fe and Co. We tested both catalysts at 220 °C (low temperature range) and 270 °C (intermediate temperature range). We initially avoided high temperature range ($\geq$ 300 °C) because of important carbon deposition already at 270 °C. The GC measured the CO and H_2 conversion every hour (Figure 6).

For each test, conversion drops dramatically in less than 13 h on stream. In both the tests at 270 °C almost all the CO reacted during the first couple of hours then conversion dropped to below 10 %.

Coking causes this fast deactivation: the deposition of inactive carbon molecules on Fe blocks the active sites [39]. At 270 °C, the monometallic and bimetallic catalyst deactivate under 13 h, but the conversion is unstable. Coking probably creates preferential paths in the catalytic bed, which redirect the reagents to fresh catalyst areas, hence yielding unstable CO conversion.

ACCEPTED MANUSCRIPT

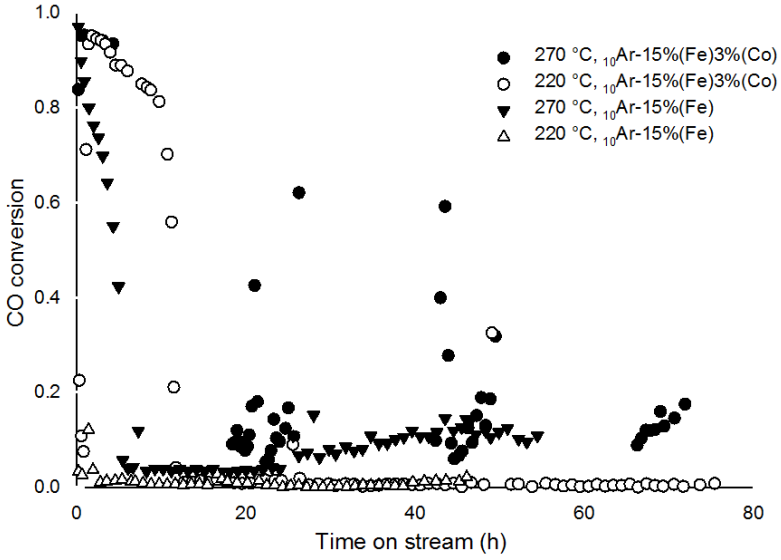

Figure 6: CO conversion measured by the GC. $H_2/CO = 2$, $P = 300\,\text{psi}$, $Q_{in} = 810\,\text{SmL/min}$, $V_{cat} = 13.5\,\text{mL}$, $\tau = 1.0\,\text{s}$

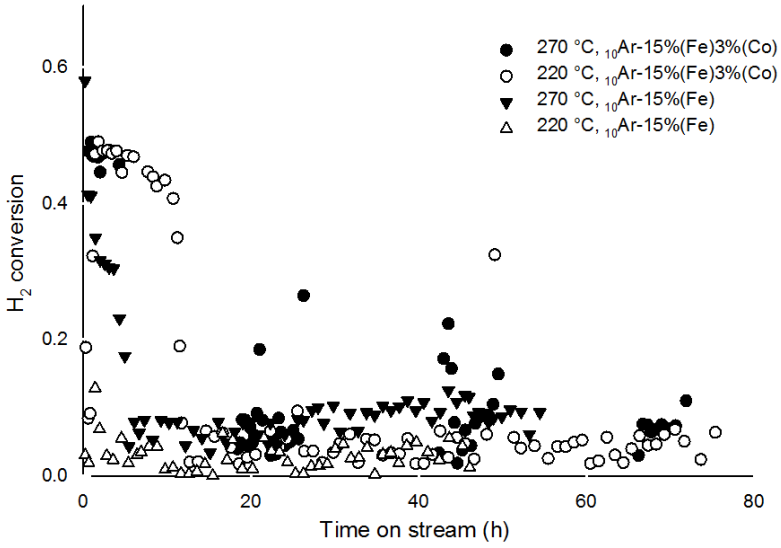

Figure 7: H_2 conversion measured by the GC. $H_2/CO = 2$, $P = 300\,\text{psi}$, $Q_{in} = 810\,\text{SmL/min}$, $V_{cat} = 13.5\,\text{mL}$, $\tau = 1.0\,\text{s}$

ACCEPTED MANUSCRIPT

Table 4: Catalytic activity of $_{10}$Ar-15%(Fe)3%(Co) and $_{10}$Ar-15%(Fe) at 220 °C and 270 °C. (*) At 220 °C, $_{10}$Ar-15%(Fe) was inactive for the Fischer-Tropsch reaction.

Catalyst		Test temperature (°C)	Active period (h)	Liquid oil production (mL)	alpha value
% Fe	% Co				
15	3	270		10	0.79
15	3	220	12.5	< 0.1	–
15	0	270	6	25	0.79
15	0	220	0*	–	–

At 220 °C, CO conversion for the sample $_{10}$Ar-15%(Fe)3%(Co) is close to 100 % during the first couple hours of reaction, then drops to remain below 1 % after 760 min. The Budouard reaction produces coke that deactivates the catalyst. At 220 °C, the Fe based monometallic catalysts were inactive with no liquid products (Table 4).

We performed TGA analysis on sample $_{10}$Ar-15%(Fe)3%(Co) (Figure 8). Coke represented 80 % of the mass of catalyst. Oxygen removed coke effectively, and the catalyst returned to its original appearance.

3.3. Experimental tests: set B

Set B refers to experiments with a residence time of 3 s. $_{10}$Ar-15%(Fe) produced the most hydrocarbons of all tests in set A, so we chose this catalyst for set B of experiments. We compared $_{10}$Ar-15%(Fe) before and after regeneration with oxygen at 400 °C (Figure 9). During regeneration, the local temperature inside the reactor

ACCEPTED MANUSCRIPT

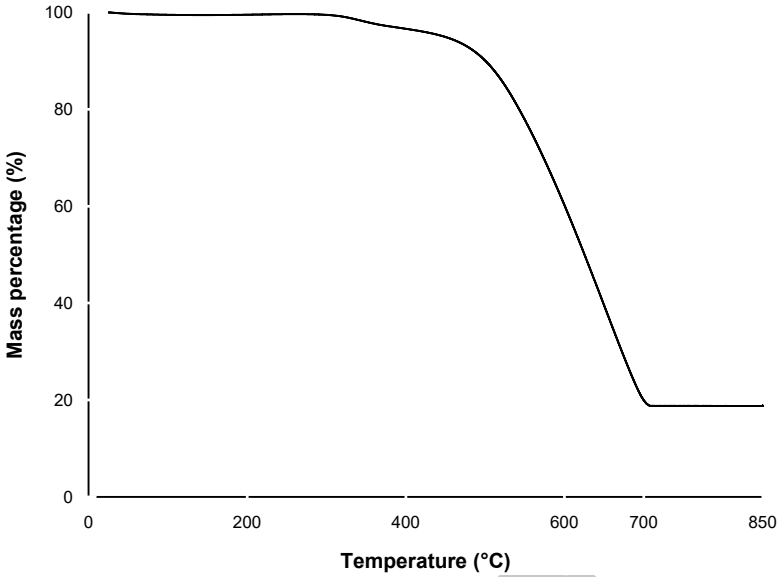

Figure 8: TGA profile of sample $_{10}$Ar-15%(Fe) after test at 270 °C

rose up to 600 °C, which likely sintered the catalyst: the average CO conversion was 3 times lower after regeneration than before regeneration.

Because of the high enthalpy of carbon combustion, we recommend regenerating similar catalysts with lower oxygen flow rates. We increased the residence time to 3 s and tested $_{10}$Ar-15%(Fe) at 270 °C and 300 °C, with all other conditions being identical to experiments of set A. CO conversion remained stable: X_{CO} was higher than 65 % after 5 days on stream (Figure 11).

At 270 °C, and $t = 72$ h the average CO conversion dropped from 80 % to 67 %. Both tests at 270 °C and 300 °C show low average H_2 conversion (20 %) as a result of the water gas shift reaction. **(author?)** [40] showed that carbon deposition rate

ACCEPTED MANUSCRIPT

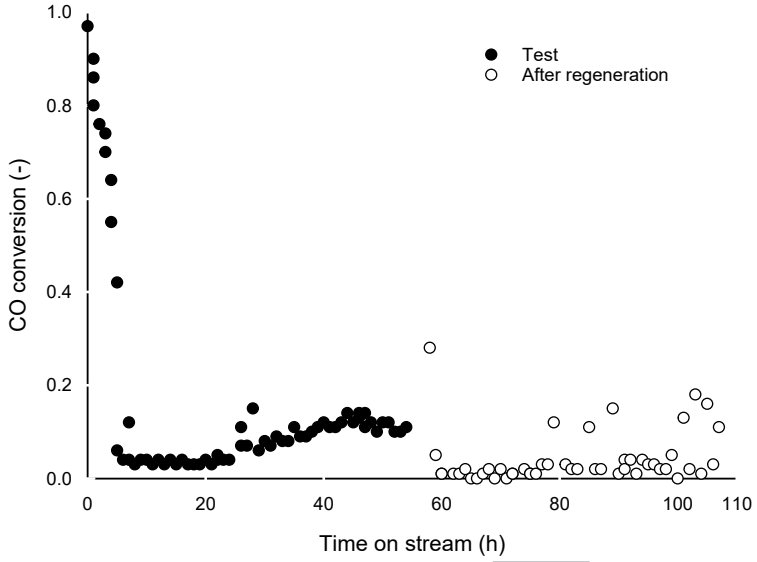

Figure 9: CO conversion for $_{10}$Ar-15%(Fe) before and after regeneration with oxygen at 400 °C. H_2/CO= 2, $P = 300$ psi, $Q_{in} = 810$ SmL/min, $V_{cat} = 13.5$ mL, $\tau = 1.0$ s.

is proportional to $\frac{P_{CO}}{(P_{H_2})^2}$, hence hydrogen protects the catalyst from deactivation.

The α value characterizes the total amount of products obtained at the end of the test. $\alpha_{270\,°C}$ and $\alpha_{300\,°C}$ are very similar (0.63 and 0.64) (Figure 10). Those values agree with the work of **(author?)** [41] on Fe catalyst at high temperature.

The conversion of CO increases by 3 % when increasing the temperature from 270 °C to 300 °C. The selectivity towards CO_2 reaches 35 % in both tests (Table 6), which indicates that the water gas shift reaction is active (Eq. 2). The selectivity towards CH_4 is slightly higher than what predicted by the ASF model, which is a usual deviation for Fe catalysts [12].

ACCEPTED MANUSCRIPT

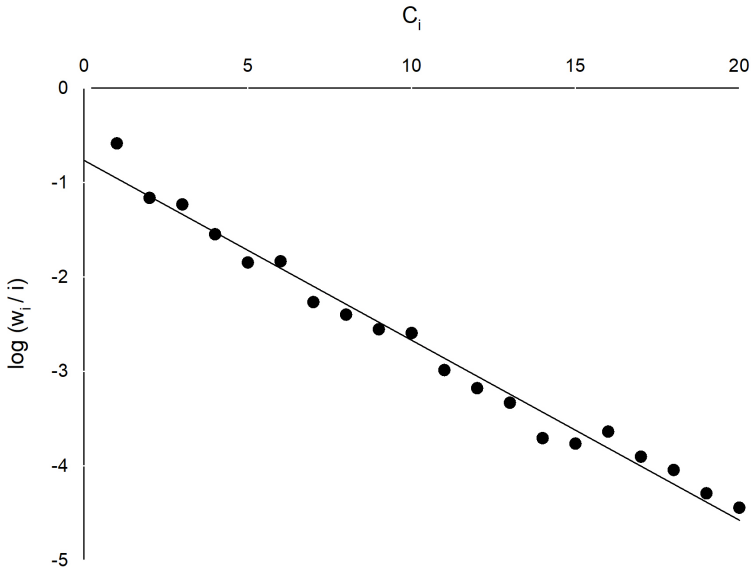

Figure 10: ASF plot after 70 h on stream. Catalyst $_{10}$Ar-15%(Fe), temperature 300 °C. The slope of the linear regression is -0.1905. The α parameter is deduced from this value: $\alpha = 10^{-0.1905} = 0.64$.

$$CO + H_2O \longleftrightarrow CO_2 + H_2. \tag{2}$$

We performed our test at higher temperature than Pirola et al. [21], and obtained higher selectivity to CH_4 as well as higher yield to C_{2+} products. Steynberg et al. observed the same trend [42]. On the other hand, our selectivity to $C_8{}^+$ products is lower. This limitation could be overcome by adjusting the proportions of promoters in favour of heavy products formation. The activation procedure possibly limited catalyst activity: **(author?)** [35] reported that iron carbides are the main active phase for Fischer-Tropsch synthesis. Activating the Fe catalyst in syngas for future

ACCEPTED MANUSCRIPT

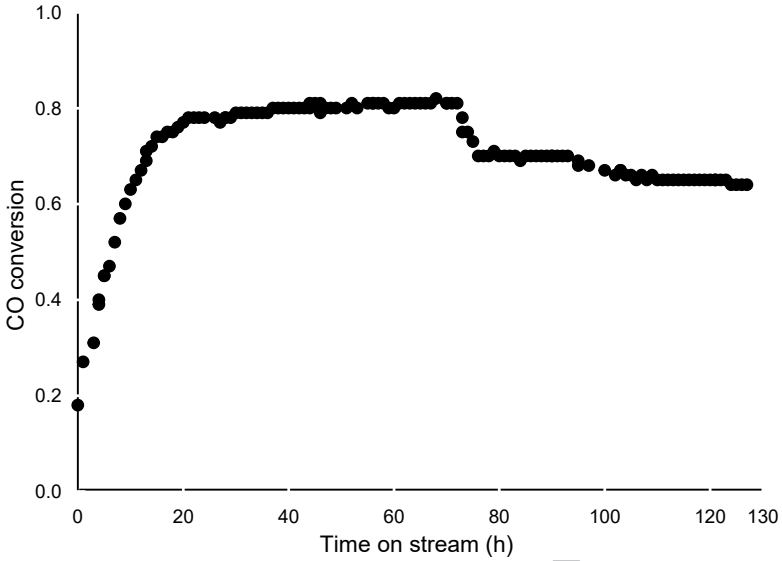

Figure 11: CO conversion for $_{10}$Ar-15%(Fe) at $T = 270\,°C$.
$H_2/CO = 2$, $P = 300\,\text{psi}$, $Q_{in} = 263\,\text{SmL/min}$, $V_{cat} = 12.9\,\text{mL}$, $\tau = 2.9\,\text{s}$.

Table 5: Experimental results for $_{10}$Ar-15%(Fe) tests at 270 °C and 300 °C: mass balance, α value and conversion rate. The mass balance is expressed on a carbon atom basis.

	270 °C	300 °C
Mass balance	99 %	99 %
Chain growth probability α	0.63	0.64
CO conversion rate ($\text{mol g}^{-1}\,\text{h}^{-1}$)	1.19×10^{-2}	1.23×10^{-2}

catalytic tests, preferentially below 350 °C to avoid forming coke is an option [21]. Changing activation procedure would increase the concentration of carbide species at the expense of oxides and would favour the Fischer-Tropsch reaction over the water gas shift reaction [43].

ACCEPTED MANUSCRIPT

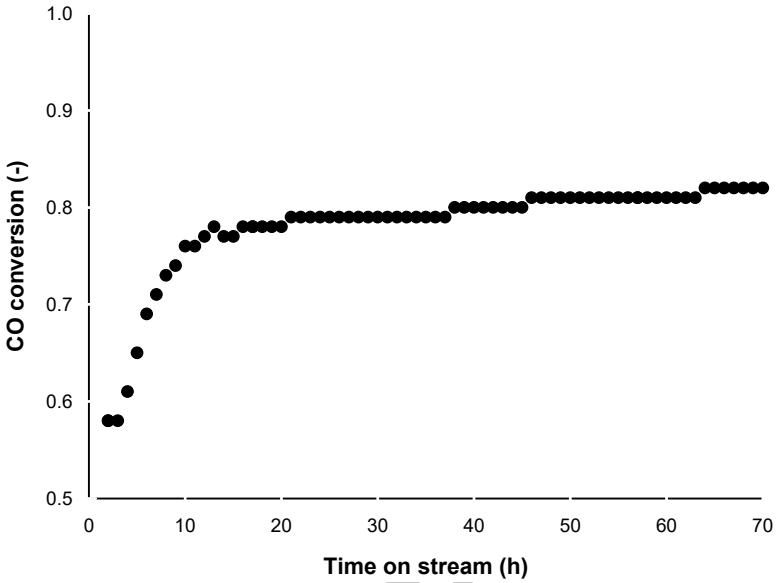

Figure 12: CO conversion for $_{10}$Ar-15%(Fe) at 300 °C.
H_2/CO= 2, $P = 300$ psi, $Q_{in} = 263$ SmL/min, $V_{cat} = 12.9$ mL, $\tau = 2.9$ s.

Table 6: Experimental results for $_{10}$Ar-15%(Fe) test at 270 °C: Selectivities, conversion and yield. Selectivities are expressed on a carbon atom basis. Yield is calculated as yield (%) = selectivity (%) $*$ conversion (%) $*$ 100.

	Selectivity (%)				X_{CO}	Total yield C_{2+}
	CH_4	CO_2	C_{2-7}	C_{8+}	(%)	(%)
270 °C	15	35	41	9	79	39
300 °C	16	34	42	8	80	40
ASF model ($\alpha = 0.64$)	12		72	17		

ACCEPTED MANUSCRIPT

4. Conclusion

We synthesized monometallic Fe-based and bimetallic Fe−Co-based catalysts for high-temperature Fischer-Tropsch reaction as the second stage of a micro-refinery unit. Sonicating the solution during impregnation effectively dispersed the active phase on the support compared to the blank sample. When Ar bubbles in presence of ultrasound, the particles have a more spherical shape and rougher outer surface compared to catalysts synthesized without Ar, but bigger particle size.

With ultrasound we reduced the total impregnation time from more than 12 h (traditional) to 4 h. The catalysts were then tested in fixed-bed for 50 h to 120 h on stream. Catalyst deactivation was fast at low residence time as a result of local elevation of temperature in favour of Boudouard reaction. Increasing residence time to 3 s stabilized the catalytic behaviour, giving CO conversion 80 % and yield to C_{2+} of 40 %, impregnation period being three times shorter than traditional methods. The water gas shift reaction was active for both tests at 270 °C and 300 °C, the latter temperature being more favourable in the context of a micro-refinery unit. Future work should investigate the effect of reduction conditions on the performances of the catalyst, higher loadings of iron and optimization of precursor proportions in order to maximize liquid products selectivity.

ACCEPTED MANUSCRIPT

Acknowledgements

We express our gratitude to Benedetta Sacchi for performing XPS measurements at University of Milan. We are thankful to the Foundation of Polytechnique Montrál for the start-up grant for new professors. The authors acknowledge the support of the Natural Sciences and Engineering Research Council of Canada (NSERC). This research was financed, in part, thanks to funding from the Canada Research Chairs program.

ACCEPTED MANUSCRIPT

ACCEPTED MANUSCRIPT

References

[1] Z. Rui, P. A. Metz, D. B. Reynolds, G. Chen, X. Zhou, Historical pipeline construction cost analysis, Int. J. Oil Gas Coal T. 4 (3) (2011) 244–263.

[2] Zero routine flaring by 2030, World Bank., http://www.worldbank.org/en/programs/zero-routine-flaring-by-2030 (accessed 18 May 2018).

[3] C. Trevisanut, S. M. Jazayeri, S. Bonkane, C. Neagoe, A. Mohamadalizadeh, D. C. Boffito, C. L. Bianchi, C. Pirola, C. G. Visconti, L. Lietti, et al., Micro-syngas technology options for GtL, Can. J. Chem. Eng. 94 (2016) 613–622.

[4] G. Patience, D. Boffito, Method and apparatus for producing chemicals from a methane-containing gas, uS Patent 9,243,190 (Jan. 26 2016).

[5] Z. Ma, P. Ouzilleau, C. Trevisanut, C. Neagoe, S. Lotfi, D. C. Boffito, G. S. Patience, Partial oxidation of methane to syngas over Pt/Rh/MgO catalyst supported on fecralloy woven fibre, Can. J. Chem. Eng. 94 (4) (2016) 642–649.

[6] S. Mousavi, A. Zamaniyan, M. Irani, M. Rashidzadeh, Generalized kinetic model for iron and cobalt based Fischer–Tropsch synthesis catalysts: Review and model evaluation, Appl.Catal., A 506 (2015) 57 – 66. doi:http://dx.doi.org/10.1016/j.apcata.2015.08.020.

ACCEPTED MANUSCRIPT

ACCEPTED MANUSCRIPT

[7] M. E. Dry, The Fischer–Tropsch process: 1950–2000, Catal. Today 71 (3) (2002) 227–241.

URL http://www.sciencedirect.com/science/article/pii/S0920586101004539

[8] A. Raje, R. Espinoza, Method for improved Fischer–Tropsch catalyst stability and higher stable syngas conversion, US Patent 7,045,554 (May 16 2006).

[9] B. H. Davis, Fischer–Tropsch synthesis: Comparison of performances of iron and cobalt catalysts, Ind. Eng. Chem. Res. 46 (26) (2007) 8938–8945.

[10] S. Li, S. Krishnamoorthy, A. Li, G. D. Meitzner, E. Iglesia, Promoted iron-based catalysts for the Fischer–Tropsch synthesis: design, synthesis, site densities, and catalytic properties, J. Catal. 206 (2) (2002) 202–217.

[11] A. Y. Khodakov, W. Chu, P. Fongarland, Advances in the development of novel cobalt Fischer–Tropsch catalysts for synthesis of long-chain hydrocarbons and clean fuels, Chem. Rev. 107 (5) (2007) 1692–1744.

[12] A. Steynberg, Fischer-Tropsch technology, Vol. 152, Elsevier, Amsterdam Boston, 2004.

[13] H. Arai, K. Mitsuishi, T. Seiyama, TiO2-supported Fe–Co, Co–Ni, and Ni–Fe alloy catalysts for Fischer–Tropsch synthesis, Chem. Lett. 13 (8) (1984) 1291–1294.

ACCEPTED MANUSCRIPT

[14] V. de la Peña O'Shea, M. C. Álvarez-Galván, J. M. Campos-Martín, J. Fierro, Fischer–Tropsch synthesis on mono-and bimetallic Co and Fe catalysts in fixed-bed and slurry reactors, Appl. Catal., A 326 (1) (2007) 65–73.

[15] A. Griboval-Constant, A. Butel, V. V. Ordomsky, P. A. Chernavskii, A. Khodakov, Cobalt and iron species in alumina supported bimetallic catalysts for Fischer–Tropsch reaction, Appl. Catal., A 481 (2014) 116–126.

[16] V. R. Calderone, N. R. Shiju, D. C. Ferré, G. Rothenberg, Bimetallic catalysts for the fischer–tropsch reaction, Green Chem. 13 (8) (2011) 1950–1959.

[17] D. Duvenhage, N. Coville, Fe: Co/TiO2 bimetallic catalysts for the fischer–tropsch reaction: Part 4: A study of nitrate and carbonyl derived ft catalysts, J. Mol. Catal. A: Chem. 235 (1) (2005) 230–239.

[18] C. Pirola, A. Di Fronzo, F. Galli, C. Bianchi, A. Comazzi, F. Manenti, Biosyngas conversion by Fischer–Tropsch synthesis: experimental results and multi-scale simulation of a PBR with high Fe loaded supported catalysts, Chem. Eng. Trans. 37 (2014) 595–600.

[19] A. Comazzi, C. Pirola, C. L. Bianchi, F. Galli, M. Longhi, F. Manenti, High-loaded Fe-supported catalyst for the thermochemical BTL-FT process: Experimental results and modelling, Can. J. Chem. Eng. 94 (2015) 696–702.

ACCEPTED MANUSCRIPT

[20] D. B. Bukur, C. Sivaraj, Supported iron catalysts for slurry phase fischer–tropsch synthesis, Appl. Catal., A 231 (1) (2002) 201–214.

[21] C. Pirola, C. Bianchi, A. Di Michele, P. Diodati, S. Vitali, V. Ragaini, High loading Fe-supported Fischer–Tropsch catalysts: optimization of the catalyst performance, Catal. Lett. 131 (1-2) (2009) 294–304.

[22] D. C. Boffito, V. Crocellà, C. Pirola, B. Neppolian, G. Cerrato, M. Ashokkumar, C. L. Bianchi, Ultrasonic enhancement of the acidity, surface area and free fatty acids esterification catalytic activity of sulphated ZrO2–TiO2 systems, J. Catal. 297 (2013) 17–26.

[23] D. C. Boffito, F. Galli, C. Pirola, C. L. Bianchi, G. S. Patience, Ultrasonic free fatty acids esterification in tobacco and canola oil, Ultrason. Sonochem. 21 (6) (2014) 1969–1975.

[24] S. V. Sancheti, P. R. Gogate, A review of engineering aspects of intensification of chemical synthesis using ultrasound, Ultrason. Sonochem. 36 (2017) 527–543.

[25] D. G. Shchukin, E. Skorb, V. Belova, H. Möhwald, Ultrasonic cavitation at solid surfaces, Adv. Mater. 23 (17) (2011) 1922–1934.

[26] J. Balachandramohan, S. Anandan, T. Sivasankar, A simple approach for the

ACCEPTED MANUSCRIPT

sonochemical synthesis of Fe3O4-guargum nanocomposite and its catalytic reduction of p-nitroaniline, Ultrason. Sonochem. 40 (A) (2018) 1–10.

[27] M. Stucchi, A. Elfiad, M. Rigamonti, H. Khan, D. C. Boffito, Water treatment: Mn-TiO2 synthesized by ultrasound with increased aromatics adsorption, Ultrason. Sonochem. 44 (2018) 272–279.

[28] M. Stucchi, C. L. Bianchi, C. Argirusis, V. Pifferi, B. Neppolian, G. Cerrato, D. C. Boffito, Ultrasound assisted synthesis of Ag-decorated TiO2 active in visible light, Ultrason. Sonochem. 40 (2018) 282–288.

[29] M. Abdollahifar, M. Haghighi, A. A. Babaluo, S. K. Talkhoncheh, Sono-synthesis and characterization of bimetallic Ni–Co/Al2O3–MgO nanocatalyst: effects of metal content on catalytic properties and activity for hydrogen production via co 2 reforming of ch 4, Ultrason. Sonochem. 31 (2016) 173–183.

[30] P. N. Panahi, A. Niaei, D. Salari, S. M. Mousavi, G. Delahay, Ultrasound-assistant preparation of Cu–SAPO–34 nanocatalyst for selective catalytic reduction of NO by NH3, J. Environ. Sci. 35 (2015) 135–143.

[31] A. Comazzi, C. Pirola, M. Longhi, C. L. Bianchi, K. S. Suslick, Fe-based heterogeneous catalysts for the fischer-tropsch reaction: Sonochemical synthesis and bench-scale experimental tests, Ultrason. Sonochem. 34 (2017) 774–780.

ACCEPTED MANUSCRIPT

[32] T. Uchida, T. Kikuchi, Ultrasonic power measurement by calorimetric method using water as heating material, in: Ultrasonics Symposium (IUS), 2013 IEEE International, IEEE, 2013, pp. 1657–1660.

[33] T. N. Phaahlamohlaka, M. W. Dlamini, M. W. Mogodi, D. O. Kumi, L. L. Jewell, D. G. Billing, J. Coville, N, A sinter resistant co Fischer–Tropsch catalyst promoted with ru and supported on titania encapsulated by mesoporous silica, Appl. Catal., A 552 (2018) 129–137.

[34] N. Pernicone, F. Traina, Catalyst activation by reduction, Pure Appl. Chem. 50 (9-10) (1978) 1169–1191.

[35] J. G. Rivera de la Cruz, M. K. Sabbe, M.-F. Reyniers, First principle study on the adsorption of hydrocarbon chains involved in fischer-tropsch synthesis over iron carbides, J. Phys. Chem. B 121 (45) (2017) 25052–25063.

[36] D. Chen, Handbook on applications of ultrasound : sonochemistry for sustainability, CRC Press, Boca Raton, FL, 2012, Ch. Ultrasound-Assisted Industrial Synthesis and Processes, p. 548.

[37] K. S. Sing, Reporting physisorption data for gas/solid systems with special reference to the determination of surface area and porosity (recommendations 1984), Pure Appl. Chem. 57 (4) (1985) 603–619.

ACCEPTED MANUSCRIPT

ACCEPTED MANUSCRIPT

[38] L. Thompson, L. Doraiswamy, Sonochemistry: science and engineering, Ind. Eng. Chem. Res. 38 (4) (1999) 1218–1219.

[39] P. Forzatti, L. Lietti, Catalyst deactivation, Catal. Today 52 (2) (1999) 165–181.

[40] M. Dry, Predict carbonation rate on iron catalyst, Hydrocarbon Process Vol. 59.

[41] A. Steynberg, Chemical concepts used for engineering purposes, in: A. Steyngerg, M. Dry (Eds.), Fischer-Tropsch technology, Vol. 152, Elsevier, Amsterdam Boston, 2004, pp. 196–257.

[42] A. Steynberg, Fischer-Tropsch technology, Vol. 152, Elsevier, Amsterdam Boston, 2004, Ch. Introduction To Fischer-Tropsch Technology, p. 5.

[43] S. Abelló, D. Montané, Exploring iron-based multifunctional catalysts for fischer–tropsch synthesis: A review, ChemSusChem 4 (11) (2011) 1538–1556.

ACCEPTED MANUSCRIPT